Nanoscale

COMMUNICATION

View Article Online
View Journal | View Issue

Cite this: *Nanoscale*, 2018, **10**, 11281

Received 26th February 2018,
Accepted 25th May 2018

DOI: 10.1039/c8nr01625a

rsc.li/nanoscale

Growth mechanism of core–shell PtNi–Ni nanoparticles using *in situ* transmission electron microscopy†

Liyun Zheng, *[a,b,c] Xiaowei Zhang,[c,d] Karen C. Bustillo, [e] Yuan Yao, [f] Lixin Zhao,[a] Minggang Zhu,[b] Wei Li*[b] and Haimei Zheng *[c,g]

Controlling the growth, morphology and structure of nanocrystals is fundamental to achieving facet dependent physical and chemical properties. Core–shell PtNi–Ni nanoparticles' evolution was investigated using *in situ* liquid cell transmission electron microscopy (TEM). A two-stage growth of core–shell PtNi–Ni nanoparticles was observed. The platinum (Pt)-based binary alloy was formed initially by a thermodynamically driven process, then grown by a monomer attachment process, and then the core formed and the process was stopped by depletion of the Pt precursor, and finally the nickel (Ni) shell formed. This growth process gives a way to grow a metallic shell for novel catalysts.

Synthesis of platinum (Pt)-based nanostructures has received widespread research in recent years because the material's high electrochemical, electronic, magnetic and catalytic activity is suitable for use in many industrial applications.[1,2] Bimetallic Pt–Ni nanostructures represent an emerging class of electrocatalysts for the oxygen reduction reaction (ORR) in fuel cells. Stamenkovic *et al.*[3] found a fundamental relationship in electrocatalytic trends on Pt_3M [M = cobalt (Co), iron (Fe), nickel (Ni), titanium (Ti), vanadium(v)] surfaces between the experimentally determined surface electronic structure (the d-band centre) and activity for ORR, which explains the activity pattern of Pt_3M nanocatalysis as well as providing a fundamental basis for the catalytic enhancement of cathode catalysis. Wu and Yang[4] investigated systematically the effects of synthesis parameters such as the types of capping agent, the reducing agent, the reaction time, and synthesized Pt_3Ni using a shape controlled process and then fabricated carbon (C)-supported electrocatalysts. They found that the Pt_3Ni electrocatalysts showed an area specific activity, which depended strongly on the (111) surface fraction and this was consistent with the results of a study on Pt_3Ni extended single crystal surfaces. Cui *et al.*[5] found an unexpected compositional segregation structure across the {111} facets, the pristine Pt_xNi_{1-x} nano-octahedra feature a Pt-rich frame along their edges and corners, whereas their Ni atoms are preferentially segregated in their {111} facet region. They investigated their morphological and compositional evolution in electrochemical environments and correlated this with their exceptional catalytic activity and found that segregation and leaching mechanisms revealed the complexity with which shape selective nanoalloys form and evolve under reactive conditions. Yu *et al.*[6] investigated the monodisperse MPt [M = Co, copper (Cu), Fe, Ni, zinc (Zn)] nanoparticles using a simple oleylamine reduction process with $M(acac)_2$ and $Pt(acac)_2$ (acac = acetylacetonate). They found that Co–Pt nanoparticles showed composition dependent structural and magnetic properties. Huang *et al.*[7] fabricated a surface-doped Pt_3Ni octahedral structure supported on C with transition metals, M-Pt_3Ni/C, such as Co, chromium (Cr), Fe, manganese (Mn), molybdenum (Mo), rhenium (Re), tungsten (W) and V. They found that Mo-Pt_3Ni/C showed the best ORR performance and stability. Despite extensive studies to design the composition, shape selective, surface decoration, structures for improved functions, the key objective in fuel cell technology to improve and reduce Pt loading as an oxygen reduction catalyst was still not satisfactory. In this research, a growth trajectory of the PtNi/Ni core–shell nanoparticle with a lower amount of Pt using *in situ* liquid cell TEM is shown.

Core–shell Pt-based nanoparticles possess superior catalytic or magnetic performance as a function of their different geometric and electronic structures.[8,9] Considerable attention has been paid to core–shell nanostructures such as Pt_3Ni@Pt_3Pd,[9]

[a]College of Materials Science and Engineering, Hebei University of Engineering, Handan, Handan 056038, China. E-mail: zhengliyun@126.com
[b]Division of Functional Materials, Central Iron and Steel Research Institute, Beijing 100081, China. E-mail: weili@cisri.com.cn
[c]Materials Sciences Division, Lawrence Berkeley National Laboratory, Berkeley, California 94720, USA. E-mail: hmzheng@lbl.gov
[d]Department of Electrical Engineering and Computer Science, Ningbo University, Ningbo 315211, China
[e]National Center for Electron Microscopy, Molecular Foundry, Lawrence Berkeley National Laboratory, Berkeley, California 94720, USA
[f]Institute of Physics, Chinese Academy of Science, Beijing 100190, China
[g]Department of Materials Science and Engineering, University of California, Berkeley, California 94720, USA

†Electronic supplementary information (ESI) available. See DOI: 10.1039/c8nr01625a

Pt-CoO,[10] Pt-Fe_2O_3,[11] FePt-$CoFe_2O_4$,[12] FePt-Fe_3O_4,[13] Ni@Pt[14] nanoparticles. But the formation mechanisms of Pt-based core–shell nanostructure systems[15] are mostly discussed based on post-reaction investigations. There are still many fundamental questions in the field of core–shell nanoparticle colloidal synthesis. For example, what are the possible growth pathways for core–shell formation? What conditions are necessary to form core–shell nanoparticles and then get a metallic shell? What is the nature of the interface between the core and the shell? Even the simple Pt-based binary single crystal nanoparticle's growth mechanism is not clearly understand yet.

In situ liquid cell TEM is a unique technique for direct imaging of nanoparticle synthesis in liquid with high spatial resolution.[16–18] Use of the technique can provide key information about the structural dynamics of a material during its nucleation, growth and transformation process.[19] Progress in the visualization of nanoparticle growth,[20] nanorod self-assembly,[21] electrochemical deposition,[22] growth of seed-mediated core–shell structures[17,18,23] and of biological materials in liquid water[24] has been made using *in situ* liquid cell TEM. Very recently Liang *et al.*[25] have demonstrated that Fe_3Pt-Fe_2O_3 core–shell particles can be formed where the growth of an Fe–Pt alloy core was followed by formation of an iron oxide (Fe_2O_3) shell. The observation suggests that Pt catalyzes the oleylamine-assisted reduction of transition metal ions to metal ($Fe^{3+} \rightarrow Fe^0$).[24] However, it is not clear if these findings apply to Pt–Ni binary alloys. In this work, utilizing *in situ* liquid cell TEM, real time structure formation and growth trajectories of PtNi–Ni and PtNi nanoparticles were imaged using electron beam induced sequential reactions in the growth solution. The PtNi–Ni core–shell particle was developed using a core–shell two-stage growth mechanism where the Ni : Pt ratio was 4 : 1.

All the chemicals were used as-received from Sigma-Aldrich Co., including $Pt(acac)_2$ (99%), $Ni(acac)_2$ (99%), oleylamine (98%), oleic acid(99%), and benzyl ether(99%). The growth solution used was 0.3 mmol of $Pt(acac)_2$ and $Ni(acac)_2$ in total as precursors. The ratio between $Ni(acac)_2$ and $Pt(acac)_2$ precursors were 4 : 1 and 1 : 1. The precursors were dissolved in 5.4 ml oleylamine, 0.6 ml oleic acid and 0.6 ml benzyl ether (total 6.6 ml solution). The chemicals were heated to 50 °C under magnetic stirring for 1 h to obtain an homogenous mixture. Heating slightly above room temperature facilitated dissolution but no particle growth was initiated. This uniform solution was used for liquid cell loading.

Static liquid cell devices with 15 nm thick silicon nitride membrane windows were fabricated in advance at the Marvell Nanofabrication Laboratory of the University of California at Berkeley, following the method of Zheng *et al.*[16] The precursor solution, about 100 nl, was loaded into the liquid cell *via* one of the reservoirs and this flowed through the electron transparent channel by capillary force. After loading the liquid, epoxy was used to seal the two reservoirs. Then, the sealed cell was loaded into a TEM holder. The *in situ* TEM observation of real time growth from the precursor solution was achieved through the window region of the liquid cell.

For the movies (Movies S1–S4, ESI†), a Jeol JEM 3010 TEM equipped with a Gatan Orius 833 camera recorded images at a rate of 10 frames per second. Before observation, the electron beam was focused to a convergent beam and irradiated the solution for a few minutes and then gradually the electron beam was spread. The bulk solution receded leaving a thick solution film of approximately 30 nm[16] in which the metal ions were reduced *in situ* by the solvated electrons to form nanoparticles. Once the reaction was initiated, the magnification was increased to 600 000× and recorded from this region of interest or zone. The image analysis was carried out using Image J software. The output image file was in binary format during recording and then extracted into Digital Micrograph (DM) data format.

Selected area electron diffraction (SAED) was performed using a Jeol JEM-ARM200F Cs Corrected S/TEM at the Institute of Physics, Chinese Academy of Sciences. A FEI Tecnai microscope operating at 200 kV was used for the high resolution TEM (HRTEM). Elemental X-ray maps (EDS) were acquired using a FEI Titan microscope operating at 200 kV with energy dispersive X-ray detectors and the four silicon drift EDS detectors had a solid angle of 0.7 steradian. The EDS maps were acquired using a beam current of 0.3 nA. The high-angle annular dark-field imaging – scanning transmission electron microscopy (HAADF-STEM) images were acquired at a probe convergence semi-angle (α) of 10 mrad. The *ex situ* imaging and mapping was performed after acquiring the *in situ* movies. The previously exposed liquid cell samples were dried in an ambient environment for several days and then separated in order to collect the EDS maps. The samples were immediately loaded into the TEM holder after separation, limiting the air exposure time. The Cliff–Lorimer method[26] provided by Bruker ESPRIT software was used to quantify the atomic percentage of elements in each spectrum. The composition of the nanoparticles was determined by fitting the Pt L-edge peak, the O K-edge peak and the Ni K-edge peak and using the Cliff–Lorimer factors to account for the scattering cross-sections of the X-ray peaks.[26]

To explore the relevance of the *in situ* observations to nanostructures formed in regular chemical synthesis, experiments were also performed by using the same precursors with a ratio of Ni : Pt of 4 : 1 and the same solvents as the *in situ* experiments. The reaction solutions were placed in a three-neck round-bottom flask equipped with a magnetic stirrer, a reflux condenser, a thermometer and a rubber septum. The reaction was performed under a nitrogen atmosphere and the reaction mixture was heated to 180 °C and refluxed for 30 min, after which it was cooled to room temperature and then washed using a polar solvent (ethanol) followed by washing with a non-polar solvent (hexane).

During the *in situ* TEM, the growth trajectory of the core–shell PtNi–Ni nanoparticles was observed in the main area of the liquid cell window (Fig. 1A, and Movie S1, ESI†). These core–shell PtNi–Ni nanoparticles have a different growth process to that reported for iron platinum–iron oxide (Fe_3Pt-Fe_2O_3).[25] The first Pt clusters' nucleation was initiated by focusing the electron beam to 5–9 × 10^4 A m^{-2}. The reduction

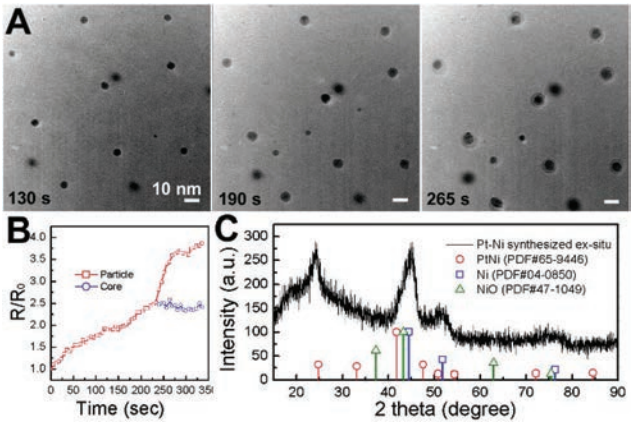

Fig. 1 Growth trajectory of nanoparticles in precursor solution with a Ni : Pt ratio of 4 : 1 and an electron dose of 3120e^- Å^{-2} s^{-1}. (A) Sequential images captured during the growth at 130 s, 190 s and 265 s, and (B) trace for the growth kinetics of the core–shell nanoparticle. (C) XRD pattern of PtNi–Ni nanoparticles synthesized outside the microscope without the electron beam assisting the growth.

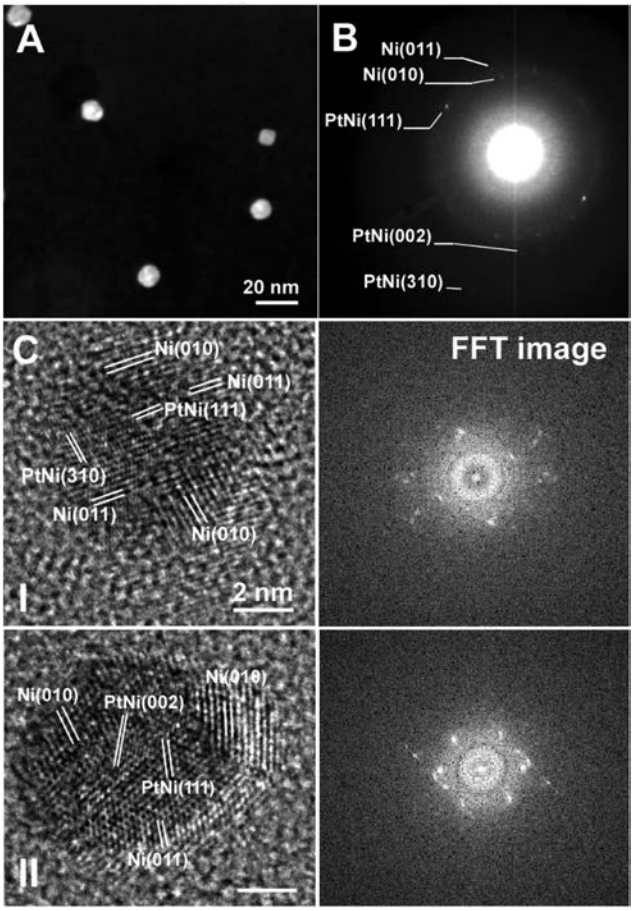

Fig. 2 (A) STEM, (B) SAED and (C) HRTEM images of the core–shell nanoparticles synthesized in precursor solution with a Ni : Pt ratio of 4 : 1 and an electron dose of 3120e^- Å^{-2} s^{-1} in the microscope.

of Pt^{2+} ions to Pt metal can be from either oleylamine assisted metal ion reduction or reduction by the solvated free electrons from inelastic scattering of the incident electron beam.[16] Oleylamine also acted as a reduction agent with Pt atom catalyzation to reduce Ni^{2+} ions and form PtNi alloy nanoparticles. When the Pt was depleted in the precursor solution, the core size was defined and then the Ni sheath forms. It was noted that the shell was very uniform, which indicated that the process was under thermodynamic control and the atom could diffuse and migrate to reduce the surface free energy. Furthermore, the Ni shell formation process was very similar to the synthesis of Ni nanoparticles reported in the literature,[27–29] where the precursor was $Ni(acac)_2$ and the solvents were oleylamine, oleic acid and trioctylphosphine or borane tributylamine. The Ni metal shell was formed rather than NiO because the Ni nanostructures require higher temperatures for significant conversion to nickel(II) oxide (NiO) in comparison to the oxidation of Fe and Co nanostructures.[30,31]

Fig. 1B shows the continuous growth trajectory of nanoparticles in precursor solution with a Ni : Pt ratio of 4 : 1 and an electron dose of 3120e^- Å^{-2} s^{-1}. The kinetics of particle growth follows $R/R_0 \sim t^{\beta}$, where R is the radius of nanoparticle, R_0 is the critical radius of the nuclei of the nanoparticle, and β is the growth exponent.[32] The average growth exponent, β, was calculated to be approximately 0.37, which obeyed the diffusion-limited growth of the Lifshitz–Slyozov–Wagner model.[32] Fig. 1C shows the X-ray diffraction (XRD) patterns of the *ex situ* nanoparticles synthesized without the assistance of the electron beam. We can obtain the PtNi–Ni nanoparticles using *ex situ* method without the radiation of electron beam. The obtained nanoparticles have the same phase structure as we get with the radiation of electron beam in the microscope.

Fig. 2 shows the STEM and SAED images of the core–shell nanoparticles synthesized in the precursor solution with a Ni : Pt ratio of 4 : 1 and an electron dose of 3120e^- Å^{-2} s^{-1}. The analysis of the SAED and HRTEM image indicated that these core–shell nanoparticles were PtNi–Ni.

Fig. 3 shows the STEM image of a PtNi–Ni nanoparticle grown from precursor solution and the Pt–Ni core has a bright contrast and the Ni sheath has gray contrast. The STEM contrast arises from both thickness and an average Z of elements. The core of the particle appears brighter than the shell indicating that the core has a higher average Z than the shell. The EDS map confirms that the core is Pt–Ni alloy and the shell is nickel as shown in the maps in Fig. 3B and C. From Fig. 3D, the oxygen EDS map, it was found that the area of the core–shell nanoparticle had a lower contrast than the surrounding area, which indicated that there was a lack of oxygen. The line scan EDS analysis was performed for a core–shell nanoparticle (Fig. 3E) and the results (Fig. 3F) also revealed the lack of oxygen of the core–shell nanoparticle.

In order to explore the beam effect on the growth mechanism, the synthesis process was performed with different electron dose rates. As is known, the hydrated electron that was injected to the reaction solution is highly reducing and respon-

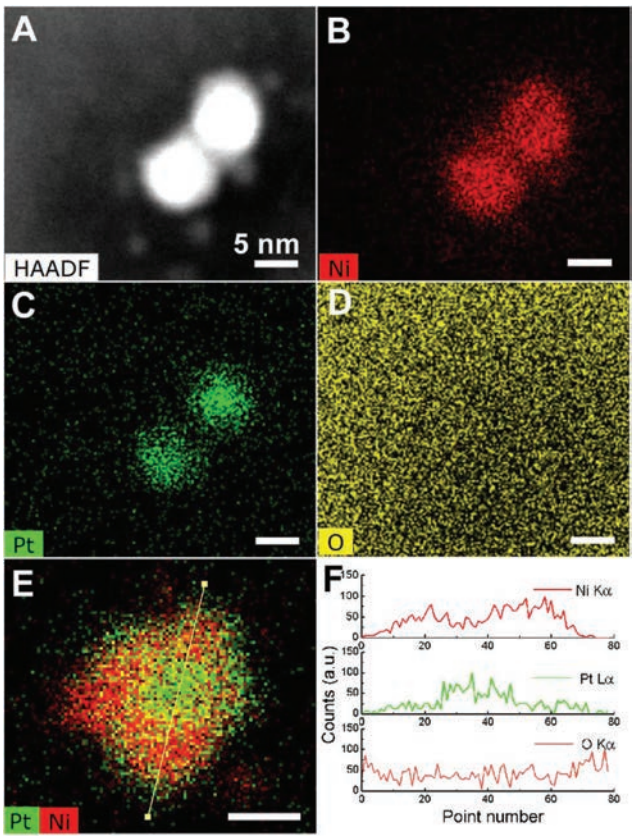

Fig. 3 (A) HAADF image, EDS element maps of (B) Ni K-edge, (C) Pt L-edge, (D) O K-edge of two core–shell nanoparticles. (E) Composite EDS maps of Ni and Pt with a line across a core–shell nanoparticle. (F) The EDS line scan analysis of the core–shell nanoparticle in (E) synthesized in precursor solution with a Ni : Pt ratio of 4 : 1 and an electron dose of 3120e^{-} Å^{-2} s^{-1}.

sible for the reduction of ions into metal atoms, inducing the nucleation and the growth of the nanoparticles that follows. Fig. 4 shows the time-lapse TEM images and growth rate of the core–shell nanostructure with a Ni : Pt ratio of 4 : 1 and different electron doses. As shown in Fig. 4A and Movie S2 (ESI†), at a low dose rate of 1500e^{-} Å^{-2} s^{-1}, spherical particles were formed. But its growth speed was very slow and showed time-evolved growth profiles (Fig. 4C), which indicated a reaction limited growth mechanism. A similar observation was previously reported by Zhang *et al.*[33] At a high dose rate of 5000e^{-} Å^{-2} s^{-1}, the nanoparticles grew rapidly and their size reached about 7 nm in the first 60 s (Fig. 4B and D and Movie S3, ESI†). Then the morphology became not so spherical and formed some hexagon or cube shapes. The formation of regular shaped nanostructures was attributed to a reaction limited growth driven by thermodynamics. After measuring and calculating, the average growth exponent, β, was approximately 0.41, and obeyed the diffusion limited growth of the Lifshitz–Slyozov–Wagner model, too.[32]

It is obvious that a PtNi–Ni core–shell nanoparticle was obtained, which was different from that obtained in the previous work on Fe_3Pt-Fe_2O_3 core–shell nanoparticles. That is, a

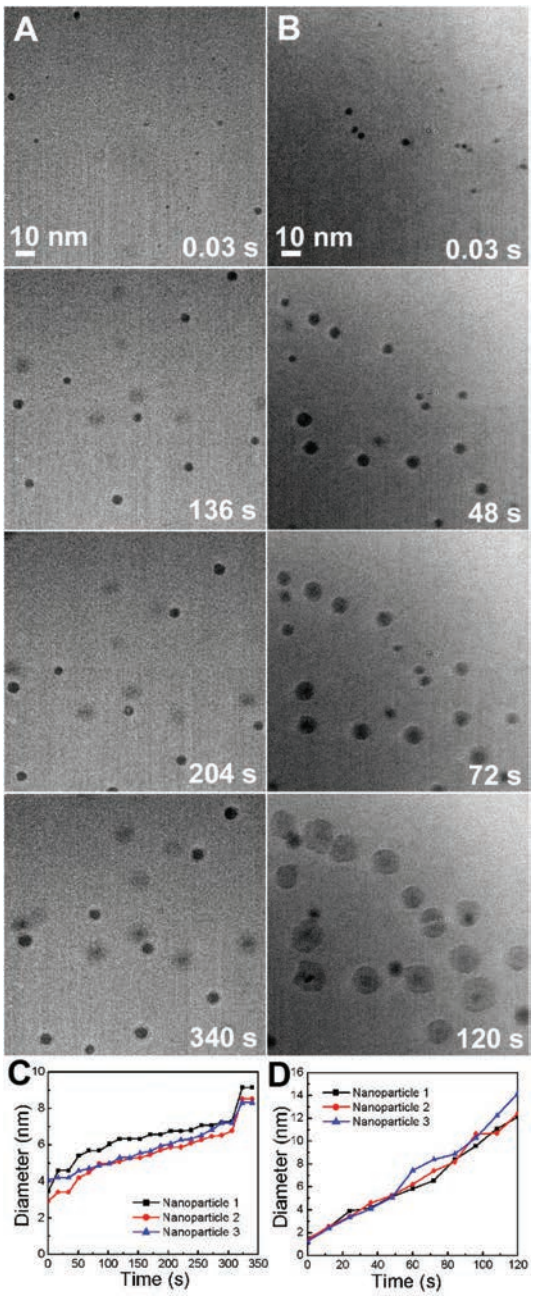

Fig. 4 (A, B) Time-lapse TEM images and (C, D) growth rate of core–shell nanostructure with a Ni : Pt ratio of 4 : 1 and electron dose of (A, C) 1500e^{-} Å^{-2} s^{-1} and (B, D) 5000e^{-} Å^{-2} s^{-1}.

Ni metallic sheath was obtained rather than an oxide sheath. These results were because of the lower amount of oxygen that was derived from oleic acid and benzyl ether in the precursor solution. In this work, the ratio of oleylamine, oleic acid and benzyl ether in the precursor solution was 9 : 1 : 1. The amount of oxygen was approximately 1.05 mmol ml^{-1}, which was much lower than that in the solution used in the research reported by Liang *et al.*[25] These results indicated that the Ni metallic atom can be obtained in a solution with a low oxygen content.

During the *in situ* TEM experiments, nucleation and growth of the PtNi nanoparticles were also observed when the ratio of Ni and Pt was 1 : 1 (Fig. 5A and Movie S4, ESI†). These nanoparticles grew by monomer attachment. All the particles still transformed into spheres during the growth process even though one particle was attached to another neighbour particle initially as a rod, which was different from the growth of PtNi rods or wires formed by coalescence in the precursor solution.

Fig. 5B shows the trace for growth kinetics of the nanoparticles in Fig. 5A. The average growth exponent of the nanoparticles, β, was calculated to be 0.07, which was much lower than that of the PtNi–Ni nanoparticles. Fig. 5C shows the size distribution of the nanoparticles synthesized by nucleation and growth. These nanoparticles have an average diameter of 6.9 nm. Fig. 5D and E shows the HAADF-STEM image and element EDS maps of a particle grown from Fig. 5A. The EDS map confirmed that the nanoparticle was a Pt–Ni alloy. Composition quantification of the nanoparticle using Cliff–Lorimer factors by fitting the Pt L-edge peak and the Ni K-edge peak showed that the Pt : Ni ratios of these Pt–Ni nanoparticles were approximately 1 : 1 (see Table S1, ESI†). Fig. 5F shows the HRTEM of the typical PtNi nanoparticles shown in Fig. 5A. The *d*-spacing values of these nanoparticles were measured and calculated and were approximately 0.2178 nm. The results of the HRTEM analysis shown in Fig. 5F suggest that the nanoparticles were cubic PtNi.

In summary, core–shell PtNi–Ni nanostructures can be synthesized using colloidal chemistry and electron beam initiation in TEM. The growth mechanism was a two-stage growth mechanism and as well as the growth of spherical PtNi nanoparticles by monomer attachment, the following Ni reduction formed the sheath of the particles. When the ratio of Ni : Pt was 1 : 1, PtNi nanoparticles were formed.

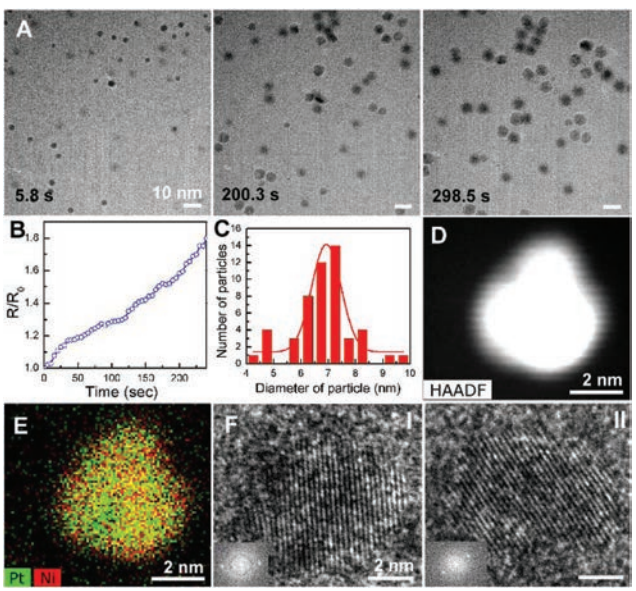

Fig. 5 Growth trajectory of nanoparticles in the precursor solution with Ni : Pt = 1 : 1. (A) Sequential images captured during the growth at 5.8 s, 200.3 s and 298.5 s, (B) trace for growth kinetics, (C) size distribution of nanoparticles, (D) HAADF image of the synthesized nanoparticles, (E) EDS maps showing Pt L-edge and Ni K-edge composite, and (F) HRTEM image for the nanoparticles from Fig. 5A.

Conflicts of interest

There are no conflicts of interest to declare.

Acknowledgements

We are grateful for the use of the Jeol JEM-3010, FEI Tecnai and FEI Titan microscopes for *in situ* and *ex situ* analysis at the National Center for Electron Microscopy, Molecular Foundry of the Lawrence Berkeley National Laboratory under the proposal of No. 3818. LZ acknowledges the support of the China Scholarship Council under No. 201408130046 and the Natural Science Foundation of Hebei Province under No. E2017402039.

Notes and references

1 W. Yu, M. D. Porosoff and J. G. Chen, *Chem. Rev.*, 2012, **112**, 5780.
2 B. Y. Xia, H. B. Wu, N. Li, N. Li, Y. Yan, X. W. Low and X. Wang, *Angew. Chem., Int. Ed.*, 2015, **127**, 3868.
3 V. R. Stamenkovic, B. S. Mun, M. Arenz, K. J. J. Mayrhofer, C. A. Lucas, G. Wang, P. N. Ross and N. M. Markovic, *Nat. Mater.*, 2007, **6**, 241.
4 J. Wu and H. Yang, *Nano Res.*, 2011, **4**, 72.
5 C. Cui, L. Gan, M. Heggen, S. Rudi and P. Strasser, *Nat. Mater.*, 2013, **12**, 765.
6 Y. Yu, W. Yang, X. Sun, W. Zhu, X.-Z. Li, D. J. Sellmyer and S. Sun, *Nano Lett.*, 2014, **14**, 2778.
7 X. Huang, Z. Zhao, L. Cao, Y. Chen, E. Zhu, Z. Lin, M. Li, A. Yan, A. Zettl, Y. M. Wang, X. Duan, T. Mueller and Y. Huang, *Science*, 2015, **348**, 1230.
8 R. G. Chaudhuri and S. Paria, *Chem. Rev.*, 2012, **112**, 2373.
9 J. Wu, M. Shi, X. Yin and H. Yang, *ChemSusChem*, 2013, **6**, 1888.
10 Y. Yin, R. M. Rioux, C. K. Erdonmez, S. Hughes, G. A. Somorjai and A. P. Alivisatos, *Science*, 2004, **304**, 711.
11 X. Teng, D. Black, N. J. Watkins and H. Yang, *Nano Lett.*, 2003, **3**, 261.
12 H. Zeng, S. Sun, J. Li, Z. L. Wang and J. P. Liu, *Appl. Phys. Lett.*, 2004, **85**, 792.
13 H. Zeng, J. Li, Z. L. Wang, J. P. Liu and S. Sun, *Nano Lett.*, 2004, **4**, 187.
14 Y. Chen, F. Yang, Y. Dai, W. Wang and S. Chen, *J. Phys. Chem. C*, 2008, **112**, 1645.
15 C. Liu, X. Wu, T. Klemmer, N. Shukla, D. Weller, A. G. Roy, M. Tanase and D. Laughlin, *Chem. Mater.*, 2005, **17**, 620.

16 H. Zheng, R. K. Smith, Y. W. Jun, C. Kisielowski, U. Dahmen and A. P. Alivisatos, *Science*, 2009, **324**, 1309.
17 K. L. Jungjohann, S. Bliznakov, P. W. Sutter, E. A. Stach and E. A. Sutter, *Nano Lett.*, 2013, **13**, 2964.
18 S. F. Tan, S. W. Chee, G. Lin, M. Bosman, M. Lin, U. Mirsaidov and C. A. Nijhuis, *J. Am. Chem. Soc.*, 2016, **138**, 5190.
19 F. M. Ross, *Science*, 2015, **350**, aaa9886.
20 H.-G. Liao, D. Zherebetskyy, H. Xin, C. Czarnik, P. Ercius, H. Elmlund, M. Pan, L. W. Wang and H. Zheng, *Science*, 2014, **345**, 916.
21 H.-G. Liao, L. Cui, S. Whitelam and H. Zheng, *Science*, 2012, **336**, 1011.
22 Z. Zeng, W.-I. Liang, H.-G. Liao, H. L. Xin, Y. H. Chu and H. Zheng, *Nano Lett.*, 2014, **14**, 1745.
23 J. Wu, W. Gao, J. Wen, D. J. Miller, P. Lu, J.-M. Zuo and H. Yang, *Nano Lett.*, 2015, **15**, 2711.
24 U. Mirsaidov, H. Zheng, Y. Casana and P. Matsudaira, *Biophys. J.*, 2012, **102**, L15.
25 W.-I. Liang, X. Zhang, Y. Zan, M. Pan, C. Czarnik, K. Bustillo, J. Xu, Y. Chu and H. Zheng, *J. Am. Chem. Soc.*, 2015, **137**, 14850.
26 R. J. Graham and J. W. Steeds, *J. Microsc.*, 1984, **133**, 275.
27 H. Winnischofer, T. C. R. Rocha, W. C. Nunes, L. M. Socolovsky, M. Knobel and D. Zanchet, *ACS Nano*, 2008, **2**, 1313.
28 S. Carenco, C. Boissière, L. Nicole, C. Sanchez, P. L. Floch and N. Mezailles, *Chem. Mater.*, 2010, **22**, 1340.
29 Ö. Metin, V. Mazumder, S. Özkar and S. Sun, *J. Am. Chem. Soc.*, 2010, **132**, 1468.
30 A. C. Johnston-Peck, J. Wang and J. B. Tracy, *ACS Nano*, 2009, **3**, 1077.
31 J. G. Railsback, A. C. Johnston-Peck, J. Wang and J. B. Tracy, *ACS Nano*, 2010, **4**, 1913.
32 I. M. Lifshitz and V. V. Slyozov, *J. Phys. Chem. Solids*, 1961, **19**, 35.
33 Y. Zhang, D. Keller, M. D. Rossell and R. Erni, *Chem. Mater.*, 2017, **29**, 10518.

